

4. REFLECTOMETRY DIAGNOSTICS FOR FUSION PLASMAS

M.E. Manso and F. Serra (Heads), L. Cupido, A. Silva, F. Nunes, I. Nunes, F. Silva, J. Santos,
L. Meneses, P. Varela, S. Vergamota, V. Grossmann, T. Ribeiro

4.1. INTRODUCTION

The main aims of this project are the design and/or implementation of reflectometry systems on ASDEX Upgrade, JET, TJ-II, MAST and ITER, as well as the development of data analysis methods and plasma physics studies based on data provided by these diagnostics.

4.2. REFLECTOMETRY ON ASDEX UPGRADE

4.2.1. Introduction

During the 2000 experimental campaign, the CFN Reflectometry Group ensured the routine operation and maintenance of both the fixed frequency channels, which monitor the density fluctuations, and the ultra fast sweeping system that measures the density profiles at both the low and high magnetic field sides.

This project included five research areas:

- Microwave circuits and electronics
- Control and data acquisition
- Data processing and evaluation
- Plasma Physics studies
- ITER relevant studies

4.2.2. Microwave circuits and electronics

4.2.2.1. Introduction

The following main activities were carried out in 2000:

- Installation of one channel in the V-band to monitor continuously the level of fluctuations at selected plasma layers.
- Development of in-phase and quadrature heterodyne detection for the above mentioned channel.
- Development of a new system for remote control of the fluctuations monitor, permitting to easily select the probing layers between shots.
- Design and construction of a new antenna with a hog horn configuration for the V-band channel, X mode, to replace the previous standard horn antenna with low gain.

- Inspection, during the ASDEX Upgrade shutdown started in August 2000, of the in-vessel waveguides circuits and antennae.
- Implementation of modifications in the antenna protections and thermal shielding.
- Assessment of the problems of the S/N ratio of the V and W-band channels.

4.2.2.2. Improvement of the dedicated fixed frequency channels

The fluctuation monitors (Q and V bands) were enclosed inside a new single cubicle, to improve the electromagnetic shielding. Each band was modified to accommodate a fixed frequency control board (to allow remote control of the frequency), so that frequencies can be set from the control room and modified between discharges.

In a first step the fluctuation monitor for the V band channel was modified to have In-phase and Quadrature (I/Q) detection, using a I/Q detector and local oscillator multiplier, developed for broadband channels, as well as PLL drives.

The system operated with proper calibration and in phase lock but the phase error resulting from this set-up is too high to be acceptable.

A careful analysis led to the following conclusions:

- The phase error resulted from the extremely poor phase noise of the main and local oscillators. Although the PLL succeeds to track the main oscillator it has some delay that gives uncorrelated differential phase noise from the main to the LO HTOs.
- The poor performance of the oscillators was identified to be:
 - (i) Intrinsic phase noise from the oscillator itself.
 - (ii) Noise by FM modulation of the HTO by the driver circuits (essentially due to the large driver bandwidth (nearly 100 MHz), required for the fast sweep application).

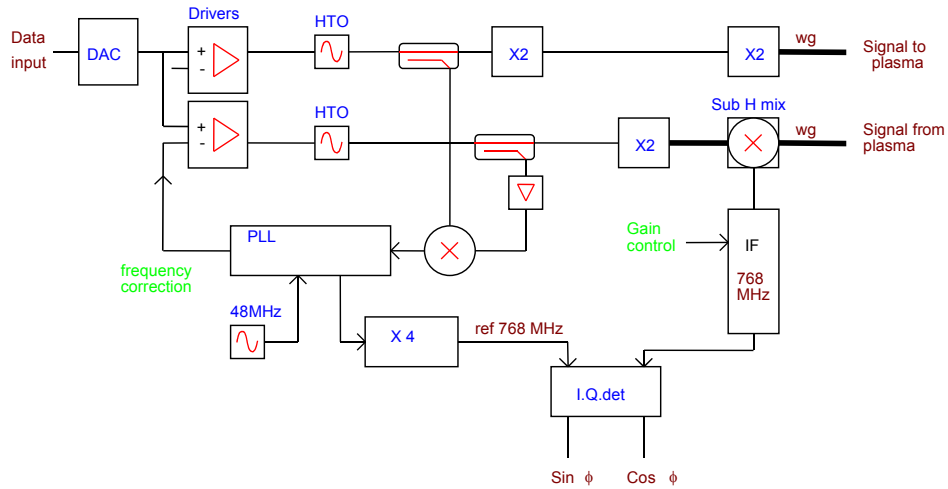


Fig. 4.1 – Schematic of the V band heterodyne fluctuations monitor.

- (iii) Noise coming from the PLL circuits (due to the loop bandwidth in excess of 20 MHz, in order to keep tracking of the HTO in the swept systems).

Two solutions were envisaged: to redesign the PLL and drivers for this application or to synthesize both HTOs frequencies to a stable external reference.

The best performance is expected using coherent signal synthesis rather than offset frequency locking (as in the broadband sections). Therefore we decided to develop an ultra wide band frequency synthesiser capable of full bandwidth frequency bands in less than 1 ms. This development is beyond the state of art.

The system is presently being developed and first tests gave promising results. It will be installed in the diagnostic by April 2001.

4.2.2.3. Improvement of the antennas

The new V band X-mode hog-horn antenna has a focal distance of 1 m, gain 20 and size 19 cm × 9.5 cm (limited by the available space < 20 cm) (Fig. 4.2).

4.2.3. Control and data acquisition

4.2.3.1. Introduction

The following main tasks were performed in 2000:

- Installation of a multiple serial port SBUS card

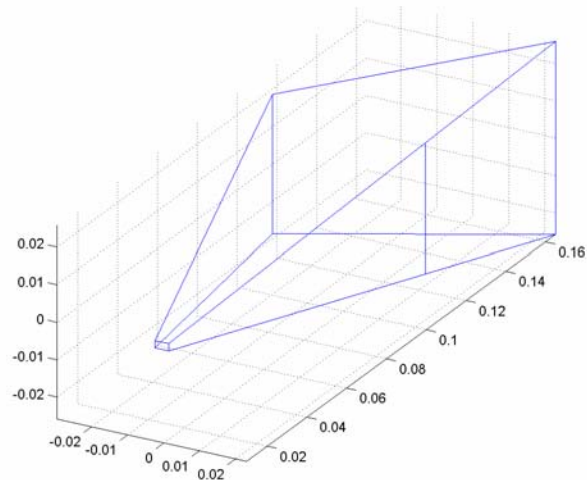
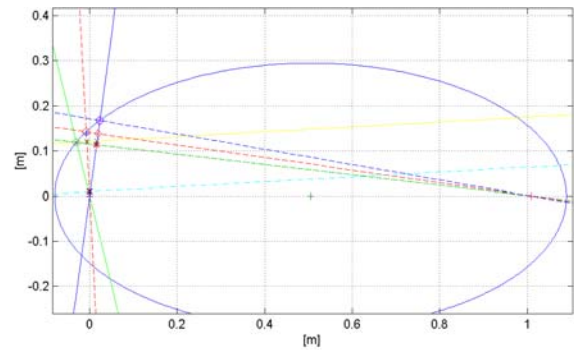


Fig. 4.2 – New ASDEX broadband microwave reflectometer V band X-mode Antenna

on the control workstation which made redundant the former control PC.

- Integration of the control software in the main configuration and software running in the workstation.

With the implemented modifications, the diagnostic can be fully operated and monitored remotely under a single unified interface from any computer connected to the internet.

4.2.3.2. System configuration

The new configuration of the reflectometry system (Fig. 4.3) includes five separate blocks: the microwave hardware; the data acquisition VME crate; the data acquisition and timing event CAMAC crate; the diagnostic workstation and the clock generation module (an arbitrary function generator (AFG)).

The VME crate has a local Master CPU board (a VME Pentium PC running Linux) that controls three 4x250 MSPS acquisition boards with 720 KB per channel, used to acquire the signals generated by the broadband system. The VME crate is connected to the control workstation (*s5ref*, as shown in Fig. 4.3), through an Ethernet connection. The CAMAC crate hosting one 2x1 MSPS (12 bits) Kynetic Systems Digitiser with 8 MB of memory per channel, is used for the fluctuation monitor. The crate also hosts a programmable pulse generator (PPG), which generates all timing events for the acquisition system.

The crate is controlled directly by *s5ref* using an SBUS-CAMAC interface board. The control workstation also interfaces with the microwave hardware through 5 serial and parallel ports. The sixth serial port control and program the AFG, which is triggered by the pulses generated by the PPG. In broadband mode, it generates the bursts of pulses that are used for sweep acquisition by the VME crate acquisition boards.

The configuration of the acquisition boards is set by the diagnostic workstation, which also programs the acquisition rate and time windows of the clock generation module. The clock pulses are sent simultaneously to the microwave sources control circuit and to the acquisition boards. After each discharge, the acquired data is sent from the VME and CAMAC crates to the diagnostic workstation to be stored in a shot-file.

The workstation is connected through three serial ports to eight programmable I/O boards that generate the control signals to set the microwave hardware according to the selected operation mode. Additionally, the parallel port of the workstation is used for switching the power of the microwave hardware and for detecting the power of the microwave hardware and for detecting timer signals from the shot. A fourth serial port is used to connect to the AFG that generates the clocks for the acquisition.

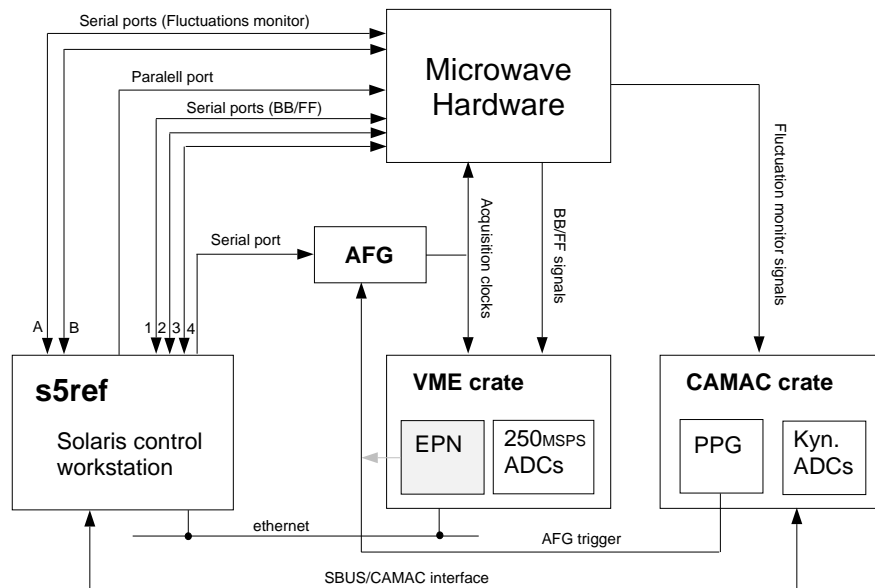


Fig. 4.3 – Block diagram of the control/acquisition system and connections to the microwave hardware

The configuration of the acquisition channels and the programming of the acquisition rates and time windows uses the diagnostic program *REF*, that runs on the diagnostic workstation and sends the necessary information to the programmable pulse generator (PPG) and to the CAMAC and VME acquisition crates. The PPG generates the acquisition time windows both in fixed frequency and broadband operation modes. In broadband each pulse sent by the PPG indicates the start of a sweep, a burst of 1024 clock pulses output by the AFG. With this burst of pulses the ramp generator board sweeps the microwave sources. In fixed frequency the PPG pulses are used directly as acquisition clocks.

The workstation opens a communication socket to the *inetd* daemon running in the VME master CPU that launches the acquisition software (*Acquire*). *REF* sends the acquisition configuration to the *Acquire* program prior to the shot initiation. The acquisition boards are then configured and armed. After the shot, the *Acquire* program writes the final data in a directory shared between the workstation and the VME crate using NFS protocol. *REF* then reads the acquired data and builds a shot-file that it sends to the ASDEX-Upgrade shot-file server.

4.2.3.3. Control software

The control software is built around a single daemon-server running on the diagnostic workstation that is responsible for every aspect of the operation.

For issuing commands to the daemon-server the operator must use a client application that is connected through an internet socket. The server accepts multiple connections, but only one has permission to make changes to the current system configuration. If another user wants to take over the operation of the diagnostic, he can send a request to the server, which will inform the current operator of this request. The operator can either accept or reject it.

Complicated tasks involving turning on various system modules, configuring and activating them, as well as changing acquisition timing configurations and signal/channel allocation to the acquisition channels are now hidden behind an intuitive and simple interface implemented in the client software.

The daemon-server is also keeping a log of every shot-file acquired by the reflectometry system. Using functions from the ASDEX-Upgrade shot-file library the program monitors the start and end of the discharges. Clients currently connected are informed that an acquisition is occurring and the system parameters may not be changed. Depicted in Fig. 4.4 is the complete control system centred on the daemon-server. A client application has been developed using IDL.

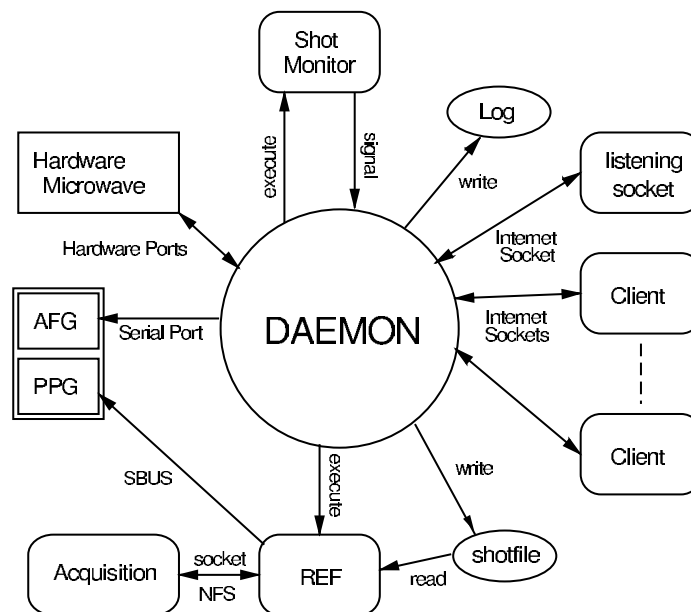


Fig.4.4 - Control/acquisition client-server architecture.

4.2.4. Data processing and evaluation

4.2.4.1. Introduction

The following main activities were performed in 2000:

- Development of software tools to enable the routine evaluation of density profiles and their availability to the users 10–15 minutes after each discharge.
- Development of software to extract automatically the temporal evolution of the radial position and density gradient at selected density layers, under the presence of plasma turbulence.
- Automatic analysis a huge amount of reflectometry data permitting to obtain the statistical properties associated with the fine temporal and spatial evolution of the density profile.

4.2.4.2. Automatic evaluation of density profiles

4.2.4.2.1. Improved profile measurements

The density profile accuracy depends heavily on the data processing tools. The key issue is the group delay (τ_g) estimation code, which is based on the best-path algorithm that uses the spectrogram of the reflected signals. Fig. 4.5 shows two examples of spectrograms obtained during an H-mode discharge. The spectrogram in Fig. 4.5(a) corresponds to a profile measured just before (120 μ s) ELM while Fig. 4.3(b) depicts the spectrogram at the onset of the same ELM. Fig. 4.5(c) presents the H_α emission. The red and blue lines indicate the measuring times of the profiles corresponding to Figs. 4.5(a) and 4.5(b), respectively. The group delay shown in Fig. 4.5(a) (white curve) could be well estimated due to the relative low level of turbulence while at the onset of the ELM, the τ_g curves can not be evaluated due to the strong perturbations.

An averaging procedure over several consecutive sweeps can be obtained to improve the accuracy. Typically profile measurements are performed in bursts of eight closely spaced (10 μ s) samples obtained in 20 μ s. An average profile per burst can be obtained with high temporal resolution (240 μ s). As simple averaging is too sensitive to spurious perturbations we developed a new method where the individual spectrograms are surimposed and the best path algorithm is then applied. An example is shown in Fig. 4.6, referring to the analysis of eight (561–568) consecutive sweeps of 20 μ s spaced by 10 μ s. Figs. 4.6(a) and 4.6(b) show two spectrograms

corresponding to two individual sweeps, 567 and 568, inside the burst, where the group delays (white curves) obtained using the best-path algorithm are also displayed. In sweep 567 a strong perturbation is observed in the time-frequency distribution (and in the group delay) in the frequency range 50–58 GHz, where as in the next sweep (obtained only 10 μ s later) the perturbation has disappeared. The burst mode spectrogram Fig. 4.6(c)) and the density profiles (Fig. 4.7) corresponding to the single and burst-mode analysis demonstrate the advantage of this multiple sweep analysis to obtain accurate profiles.

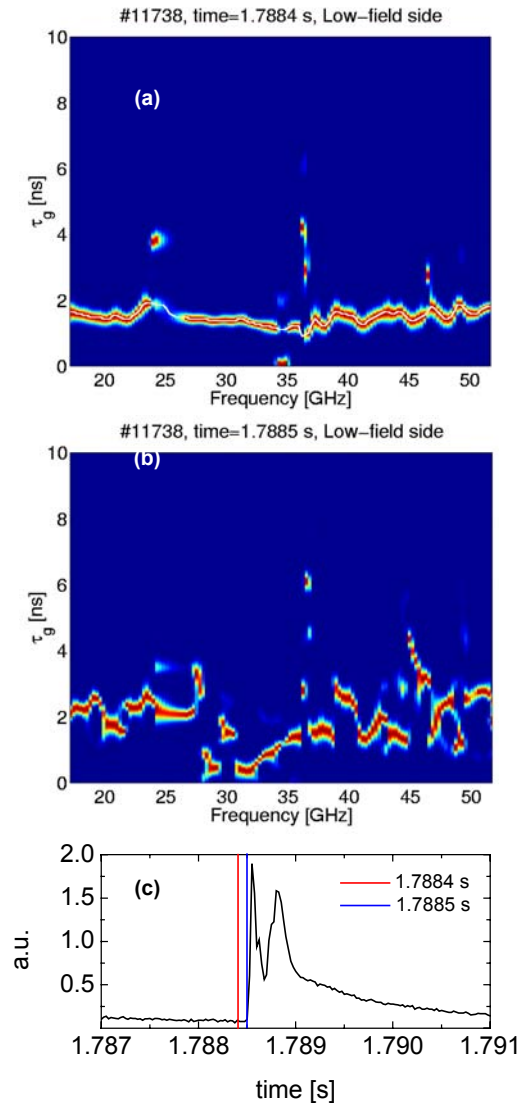


Fig. 4.5 - Examples of spectrograms obtained from 20 μ s sweeps: (a) 120 μ s before a fast ELM occurs, (b) at the onset of the ELM, and (c) H_α emission. The red and blue lines on (c) mark the measurement times of the profiles corresponding to (a) and (b), respectively.

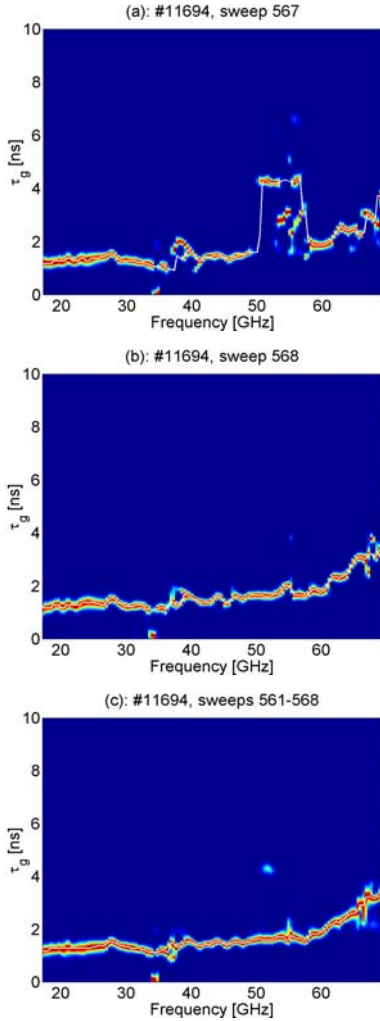


Fig. 4.6 - Example of the application of the burst-mode data analysis method to 8 (561–568) consecutive sweeps (20 s sweep time separated by 10 s) measured during an H-mode ASDEX Upgrade discharge: (a) and (b) spectrograms of two individual sweeps, 567 and 568, respectively; (c) burst spectrogram obtained with the burst-mode data analysis.

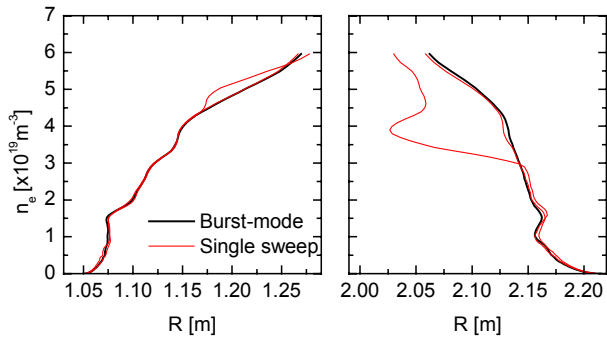


Fig. 4.7 - Density profiles from the high-field side (left) and low-field side (right) inverted using single sweep data (red curves) and with the burst-mode analysis (black curves) corresponding to the situation illustrated in Fig.4.4.

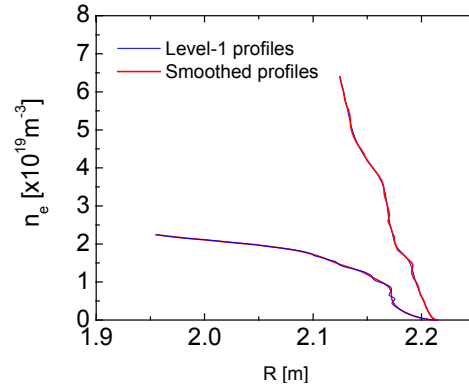


Fig. 4.8 - Application of the smoothing algorithm to two level-1 profiles.

4.2.4.2.2. Automatic routine evaluation

Reflectometry profiles are most useful if they are available in between discharges. To meet this objective a fully automatic density profile evaluation procedure was implemented that provides level-1 and level-2 profiles 10–12 minutes after each discharge. A monitoring process is launched in the background that waits for a new shot to be acquired. As soon as data is available for that shot the background process starts the level-1 and level-2 evaluation codes and proceeds to wait for the next shot. The level-2 application stays idle waiting for level-1 data to become available. When this happens the level-2 shotfile is created. To make the profiles available as quickly as possible the level-1 shot-file application subdivides itself into a number of smaller processes (typically eight): a sub set of the acquired data is given to each sub process for evaluation. At the end the results from the different sub processes are collected to create the level-1 shotfile.

Fig. 4.8 shows the measured and smoothed profiles for low- and high-density examples. In this initial implementation only profiles that become monotonic without over smoothing are stored in level-2 shot-files.

4.2.4.3. Performance of the microwave reflectometry diagnostic for density profile measurements

4.2.4.3.1. Comparison high field side / low field side
The profiles shown in Fig. 4.9 were obtained on ASDEX Upgrade shot #11711, where edge-cooling pulses are produced by injection of Si by means of Laser-Blow-Off (LBO) between 3.75 s and 5.5 s. A fast increase of the electron temperature is observed

in the centre and the confinement improves. In this discharge the reflectometry system was operated in bursts of 32 consecutive sweeps (spaced by 50 μ s) and the time interval between bursts is 100 ms.

Fig. 4.10(a) presents the evolution of the line-integrated density from the DCN interferometer. After the Si Laser Blow-Off a steepening of the density profile at both sides (measured after $t \cong 4.41$ s) occurs, in agreement with the improvement of confinement. Fig. 4.11 depicts a density profiles from the HFS after being mapped into the LFS (dashed lines) by plotting the density along the corresponding magnetic field surfaces. Good agreement is obtained with the LFS profiles (solid lines). The fact that density profiles measured with independent reflectometers (LHS/HFS), agree is a strong evidence of the great accuracy of the profile measurements.

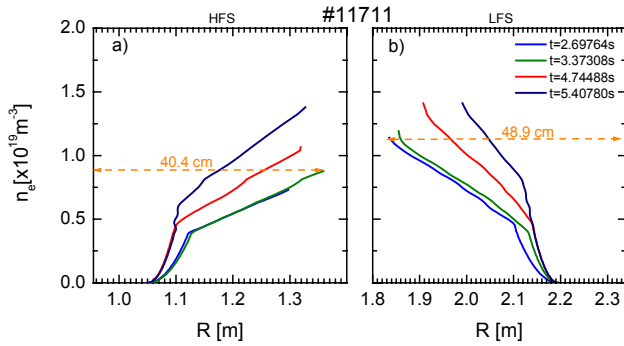


Fig. 4.9 - Electron density profiles measured from single 20 μ s microwave sweeps for shot #11711. a) High field side. b) Low field side.

Fig. 4.12(b) represents the temporal evolution of the slope of the density profile defined as

$$\text{grad} = \arctan \frac{n_e(x_2) - n_e(x_1)}{x_2 - x_1}$$

in the density region $0.5 \times 10^{19} \text{ m}^{-3}$ to $1 \times 10^{19} \text{ m}^{-3}$ and in (c) the evolution of the radial location of the plasma layer $n_e = 0.8 \times 10^{19} \text{ m}^{-3}$. In spite of the variations observed in each burst of density profiles, the expected evolution isolated, (solid line) namely the profile peaking after the improved confinement (for $t \geq 4$ s). The profile variations within each burst of profiles decreases significantly after 4 s indicating that the level of fluctuations decreased, which is typical of improved confinement.

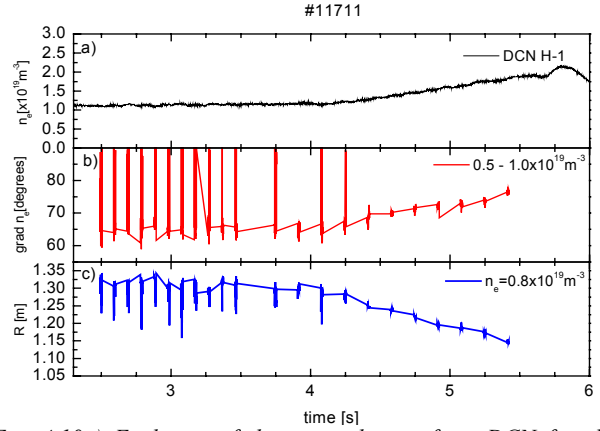


Fig. 4.10a) Evolution of the mean density from DCN for shot #11711. b) Variation of the HFS reflectometry density profiles gradient. c) Evolution of the radial position of a plasma layer seen from HFS reflectometry.

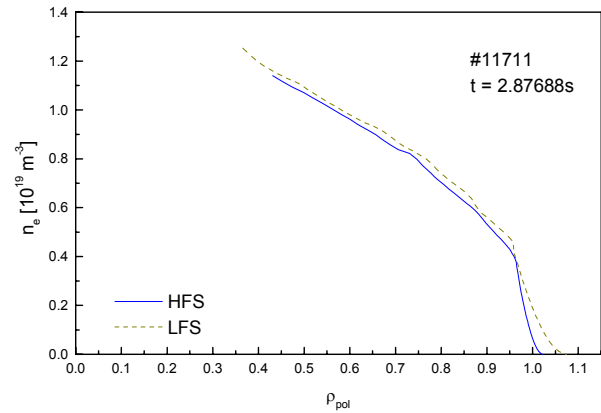


Fig. 4.11 - Mapping from the HFS profiles into the LFS, plotting the density along the corresponding magnetic field surfaces.

4.2.4.3.2. Sensitivity to plasma radial movements

The profile measurements (between 1.5 and 2.24 s), presented in Fig. 4.12 were obtained in an H-mode (shot #13171), with high density ($n_e \approx 0.1 \times 10^{20} \text{ m}^{-3}$), where the radial position of the plasma was scanned between 2.2 and 3.8 s. Fig. 4.12 shows the time-space evolution of the density profile measured by reflectometry.

From the radial changes of a density layer close to the separatrix given by reflectometry (Fig. 4.13a) and the good agreement with the plasma position inferred from the magnetic diagnostics, it is clear that reflectometry is able to follow the evolution of the plasma position. This is the first experimental demonstration that reflectometry may be used to control the plasma position as it is proposed for ITER.

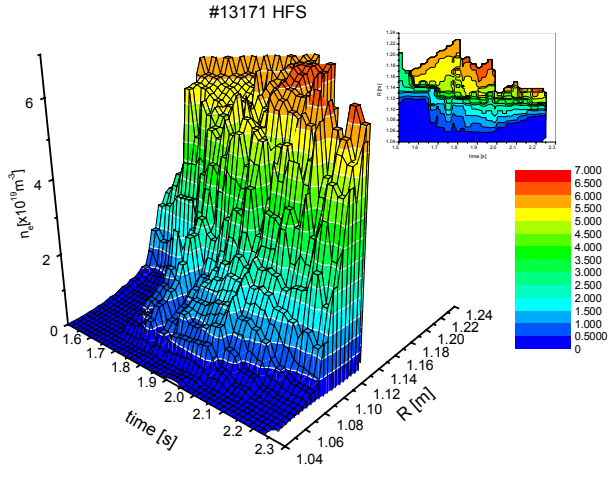


Fig. 4.12 - 3D plot of the evolution of the reflectometry density profiles for shot #13171.

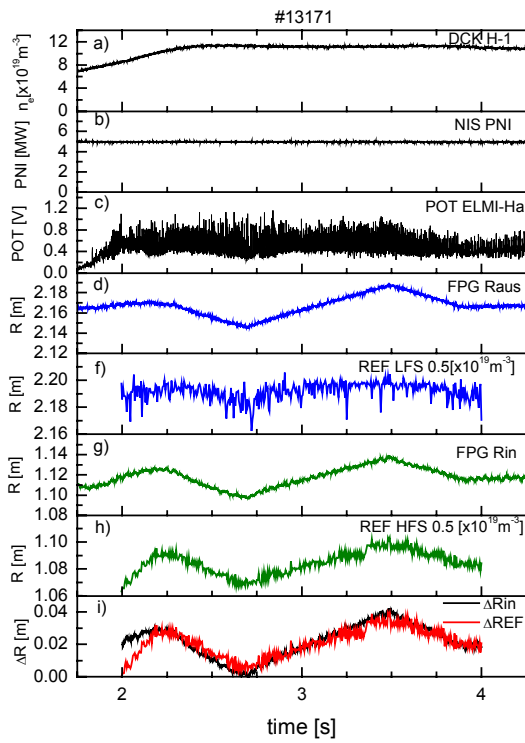


Fig. 4.13 - a) Mean density from DCN. b) Neutral beam power. c) H_α signal. d) Outer most plasma position from the magnetics. f) Position of the plasma layer $n_e=0.5 \times 10^{19} \text{ m}^{-3}$ from the LFS reflectometry profiles. g) Inner most plasma position from the magnetics. h) Position of the plasma layer $n_e=0.5 \times 10^{19} \text{ m}^{-3}$ from the HFS reflectometry profiles. i) Variation of the position from the magnetics and from reflectometry HFS.

4.2.4.3.3. Measuring range of distances and gradients
The system can cope with vertical displacements in the order of 14 cm and it can measure gradients ranging from low values Fig. 4.10(b)) to high ones (Fig. 4.14).

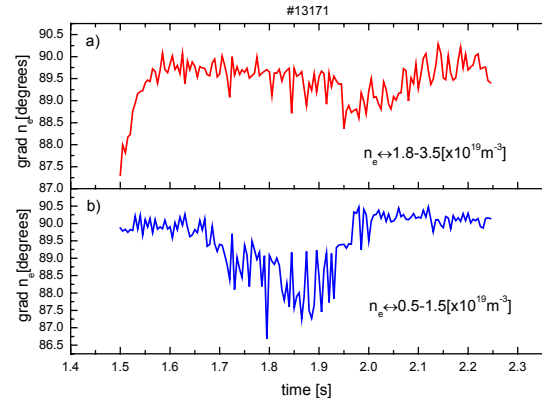


Fig. 4.14 - Evolution of the gradient of the HFS reflectometry profiles for two plasma regions.

4.2.5. Plasma Physics studies

4.2.5.1. Introduction

The following plasma physics studies have been performed:

- Study of the sustainment times during inboard pellet launch experiments
- Turbulence studies during improved confinement scenarios
- Study of turbulence during ECRH modulation experiments

4.2.5.2. Simultaneous high field/low field side density profile measurements from reflectometry during inboard pellet launch experiments

On ASDEX Upgrade an advanced fuelling method, consisting of pellet injection from the high magnetic field side (HFS), allowed particle deposition deep inside the core plasma. In these regimes the reflectometry measurements are very difficult because the pellets induce strong plasma movements and ELMs.

The experiments have been performed in similar target H mode plasmas: (a) #14023 where 13 pellets were launched (between 1.8 s and 2.6 s), with a velocity of 240 ms^{-1} and 30 Hz of repetition rate; (b) shot #14024 where 25 pellets were injected (1.8 s - 2.8 s) at 560 ms^{-1} , with the same repetition rate. The

profiles were measured each 2 ms in shot #14023 and 1 ms in shot #14024.

Fig. 4.15 depicts the temporal evolution of the group delay for a probing density $n_e=2.67 \times 10^{19} \text{ m}^{-3}$ at the LFS, in shot #14024 (dashed lines correspond to the times of the injection of the pellets). No significant effect on the group delay is observed for this density, which is located near the separatrix ($n_{e(\text{sep})} \sim 3.0 \times 10^{19} \text{ m}^{-3}$). This confirms previous results showing that the pellet injections do not affect the density profile at the plasma edge (Fig. 4.17) and do not degrade the plasma confinement.

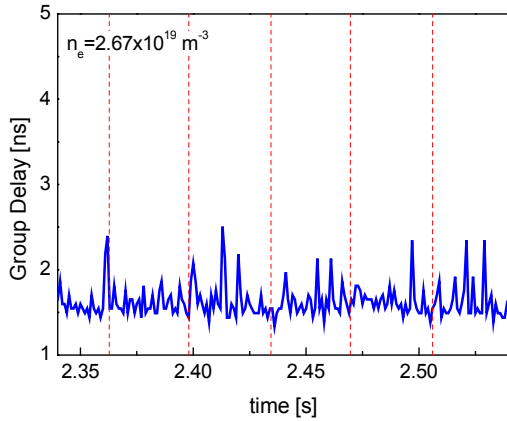


Fig. 4.15 – Temporal evolution of τ_g at LFS for a probing layer near the separatrix ($n_e = 2.67 \times 10^{19} \text{ m}^{-3}$) in discharge #14024

For higher densities (Fig. 4.16) the group delay is strongly reduced following the pellet injection associated with the peaking of the density profile (Fig. 4.17). After pellet injection, the group delay stays low during a time of typically [6 – 15] ms and after it increases revealing a flattening of the profile, which should be due to energy and particle losses. After the pellet injection the density profile peaks, both at HFS and LFS, close and inside the plasma separatrix (Fig. 4.17).

When a pellet is injected, the density layer moves outward and the decay length decrease indicating the peaking of the profile (Fig. 4.18). During some milliseconds after the pellets, the profile stiffness is maintained and after the plasma starts to flatten. This phenomena could be explained by the effects associated with strong ELM's induced by the pellets. After this confinement degradation the profile starts to recover a few milliseconds before the next pellet, peaking further when the pellet occurs.

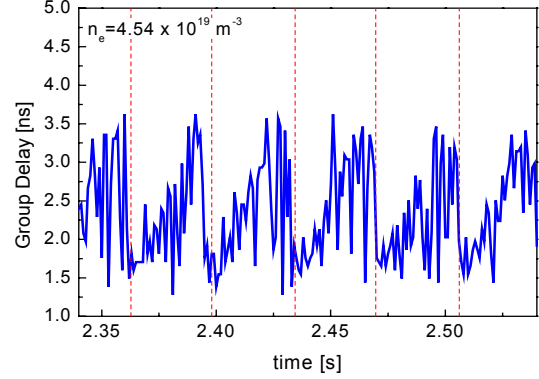


Fig. 4.16 - Temporal evolution of τ_g at LFS for a probing layer inside the separatrix ($n_e = 4.54 \times 10^{19} \text{ m}^{-3}$) in discharge #14024

Fig. 4.19 shows the sustainment time (τ) of the decay length of the density profile (estimated in the density range n_e : $[5.0 - 6.5] \times 10^{19} \text{ m}^{-3}$) after each pellet for both discharges.

A significant difference is observed at the HFS after the second pellet ($\tau \sim 8$ to 12 ms for the higher velocity and ~ 6 ms for the lower velocity). In contrast, at the low field side no clear differences are observed in the behaviour of group delay for the two different pellet velocities.

The study presented confirms previous results and suggests that increasing the pellet injection velocity the sustainment time increases at the HFS, which may indicate an improvement in the confinement.

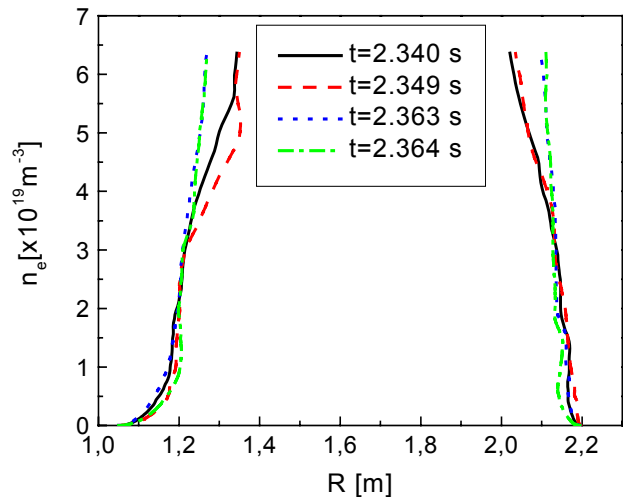


Fig. 4.17 – Density profiles evolution at HFS and LFS (#14024)

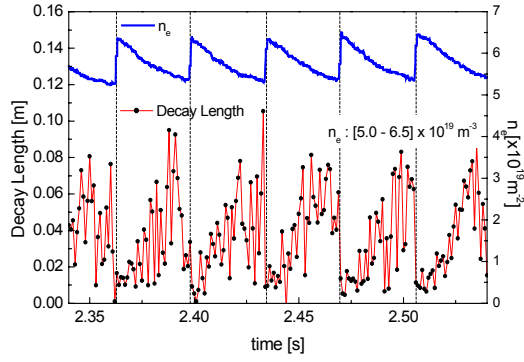


Fig. 4.18 – Evolution of the decay length at the density range $n_e = [5.0-6.5] \times 10^{19} \text{ m}^{-3}$ and the corresponding radial positions

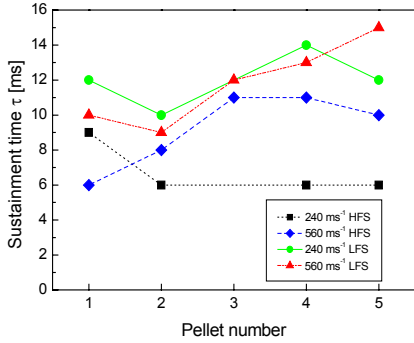


Fig. 4.19 – Sustainment time of the decay length of the density profile $n_e = [5.0-6.5] \times 10^{19} \text{ m}^{-3}$ after each pellet for discharges #14023 and #14024

4.2.5.3. Turbulence studies

The studies of plasma turbulence have been made with four channels on the LFS probing the density range $[0.3-6.5] \times 10^{19} \text{ m}^{-3}$, plus one of the two channels dedicated to study plasma fluctuations (Q-band: $[1.3-3.1] \times 10^{19} \text{ m}^{-3}$). The acquisition rate of the probing waves was $2 \mu\text{s}$. The sample interval is $\sim 1.5 \text{ s}$ for the broadband system and $\sim 8 \text{ s}$ for the dedicated fluctuation channels.

(i) H-mode with improved performance

The example presented refers to shot #13443, with improved core confinement and H-mode edge barrier. The NBI power (Fig. 4.20a) is stepped up in two stages, 2.5 MW during the plasma current ramp and 5 MW in the current flat top. Also shown is the central electron temperature T_e (b) and the D_α at the divertor (c).

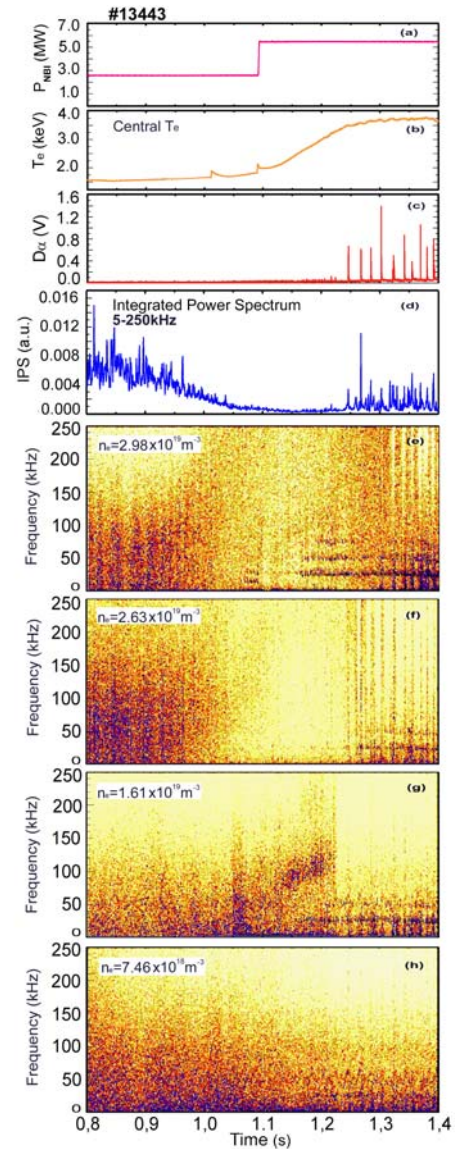


Fig. 4.20 – Temporal evolution of (a) neutral beam power; (b) central T_e ; (c) D_α at divertor; (d) IPS at $n_e = 2.63 \times 10^{19} \text{ m}^{-3}$; and contour plots of power spectra at several density layers (e), (f), (g) and (h) for ASDEX Upgrade (AUG) shot 13443. The colour scales for (e), (f), (g) and (h) are linear going from lighter to darker colours with increasing spectral intensity

Below the D_α trace are contour plots of the power spectra from reflectometer signals obtained from density layers at: (e) $2.98 \times 10^{19} \text{ m}^{-3}$; (f) $2.63 \times 10^{19} \text{ m}^{-3}$; (g) $1.61 \times 10^{19} \text{ m}^{-3}$; (h) $7.46 \times 10^{18} \text{ m}^{-3}$. Note that the colour scale in each plot has been adjusted to give maximum contrast over the available dynamic range in each spectrum. The probed layers in cases (e) and (f) are located in the density gradient region, between

normalised radius $\rho \sim 0.4$ to 0.9 (poloidal flux coordinate), while (g) is in the edge plasma, close to and inside the separatrix, and (h) in the scrape-off layer. The temporal evolution of the reflectometer cut-off layers positions have been inferred from density profiles obtained in the same discharge from Thomson scattering because all reflectometry channels were used for turbulence studies. Fig. 4.21 shows density n_e and T_e profiles at $t=1.05$ s (L-mode) and $t=1.40$ s (H-mode) phases of the discharge, while Fig. 4.22 presents the temporal behaviour of the channels during the L to H mode transition. The arrows in Fig. 4.21 indicate the O-mode cut-off densities of the reflectometer channels.

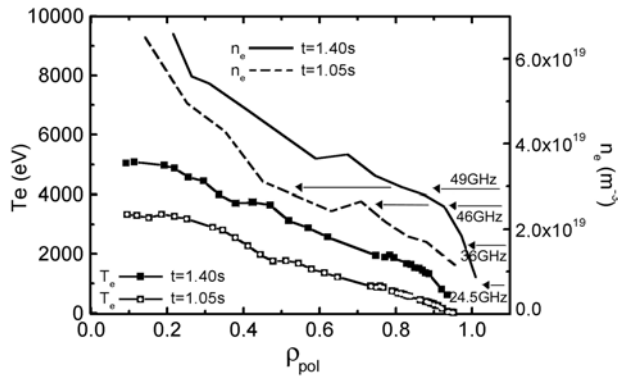


Fig. 4.21 – Electron temperature T_e (from ECE) and plasma density n_e (Thomson) radial profiles for shot 13443. Arrows indicate the location of the cut-off layers corresponding to the reflectometer channels

At the inner layers ($\rho \sim 0.4$ to 0.9) (Figs. 4.20e and 4.20f), the turbulence spectra begin to change, showing a gradual shift in the power to higher frequencies at $t \sim 1.0$ s. Integrating the power spectrum of the signal reflected at $n_e = 2.63 \times 10^{19} \text{ m}^{-3}$ in the range 5–250 kHz (Fig. 4.20d) also shows a reduction in the overall fluctuation level, coinciding with an increasing central T_e (Fig. 4.20a) and plasma stored energy W_{dia} , indicating a link between local core turbulence and plasma confinement. At this time, the toroidal rotation obtained with charge exchange spectroscopy (Fig. 4.23) shows a slight increase, followed by a more pronounced increase with the step in the neutral beam power at 1.1 s. The link between the turbulence reduction, confinement and rotation has also been seen in ITB discharges with L-mode edges. In contrast with the behaviour of the core plasma turbulence, at the edge (close and inside the separatrix (Fig. 4.20g)), the suppression of high-

frequency turbulence occurs only at formation of the H mode transport barrier at $t \sim 1.2$ s.

The inner layers (49 GHz, $n_e = 2.98 \times 10^{19} \text{ m}^{-3}$, and 46 GHz, $n_e = 2.63 \times 10^{19} \text{ m}^{-3}$) are displaced from $\rho \sim 0.4$ to 0.5 shortly before the L-H transition, to $\rho \sim 0.8$ to 0.9 (Fig. 4.22). They then enter the edge region of increased turbulence associated with the occurrence of ELMs. The broadband frequency structures typical of ELMs, can be clearly seen in Figs. 4.20e and 4.20f, after 1.25 s and in the IPS of Fig. 4.20d. In the outer edge plots they are not so clear because the level of turbulence is globally higher.

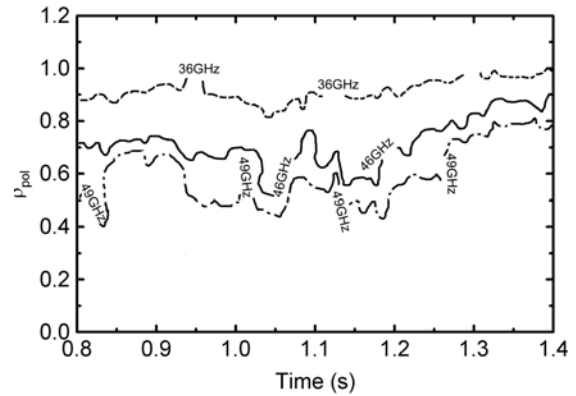


Fig. 4.22 – Temporal evolution of the cut-off layer positions for the reflectometer frequencies computed from Thomson scattering density for shot 13443 during the L to H-mode transition

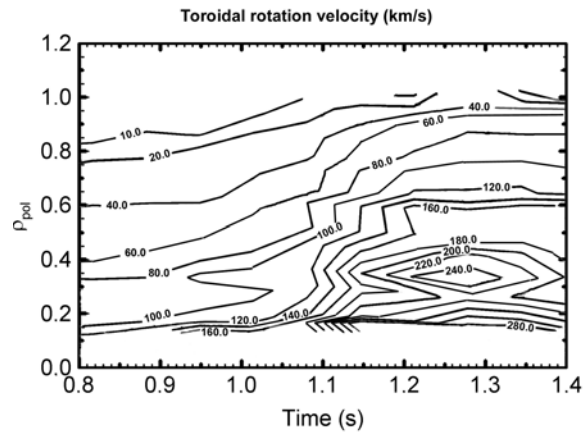


Fig. 4.23 – Contour plot of toroidal rotation velocity in km s^{-1} from Charge Exchange Recombination Spectroscopy (CXRS) versus normalized radius and time for 13443.

(ii) Reflectometry measurements during ECRH modulation experiments

Previous studies on ASDEX Upgrade indicate a step in the transport caused by Electron Cyclotron

Resonance Heating (ECRH) off-axis deposition. The step is located at the narrow (5 cm) ECRH deposition region. The microwave reflectometer has been used to study the characteristics of the density turbulence outside the deposition region during modulated ECRH.

The Ohmic discharge 13174, which has a line average density of $\sim 3.0 \times 10^{19} \text{ m}^{-3}$, where 125 kW of ECRH power was applied with a modulation frequency of 20 Hz, was analysed. The position of the probed layers relative to the ECRH deposition is shown in Fig. 4.24. There is good temporal correlation between ECRH pulses shown (Fig. 4.25a) and spectrum modulation (Fig. 4.25b) which suggests that ECRH is affecting the level of turbulence in the plasma.

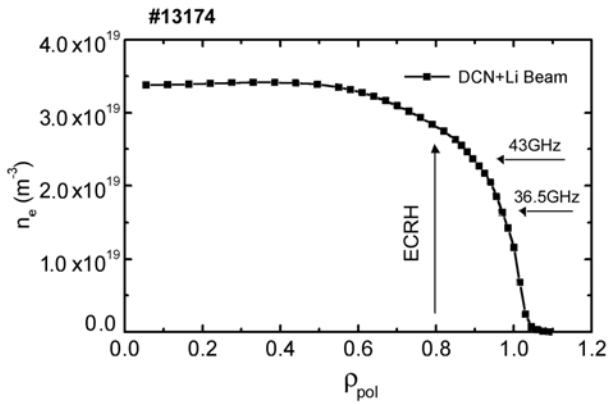


Fig. 4.24 – Density profile for discharge 13174 from DCN+Li beam interferometer versus normalized poloidal flux coordinate ρ_{pol} showing the localizations of the reflectometer 43 GHz ($n_e=2.3 \times 10^{19} \text{ m}^{-3}$) channel, 36.5 GHz ($n_e=1.65 \times 10^{19} \text{ m}^{-3}$) channel and the ECRH deposition region ($\rho_{pol} \approx 0.8$)

However, the behaviour of the modulation in the turbulence spectrum is complex. There are two distinct components in the spectrum: low frequencies from 5-20 kHz, and high frequencies above 30 kHz, which appear to have temporal behaviour out of phase with each other. When there is an enhancement in the amplitude of the low frequencies, in this case corresponding to the ECRH pulse “on”, the higher frequencies are reduced, as shown in the IPS in Figs. 4.25c and 4.25d, respectively. The same two spectral patterns are also present in other discharges with similar conditions (13177 and 12453). This distinctive spectral behaviour is not seen at cut-off layers further away from the ECRH deposition region nor in discharges without ECRH modulation. Fig. 4.26a shows the spectrum from the 36.5 GHz

reflectometry channel ($n_e=1.65 \times 10^{19} \text{ m}^{-3}$) for shot 13174, together with IPS plots for the low and high frequency ranges. This channel is located at approximately $\rho \sim 0.95$ and again shows clear modulation, except that the low and high frequency components are now in phase with each other. This “in phase” modulation appears to be due to another effect.

The homodyne reflectometer signal $S(t) = A(t) \cos(\tilde{\phi}(t) + \phi_0(t))$ depends linearly on the reflected signal amplitude (A), and non-linearly on the relative phase shift (ϕ). The phase term also contains a mean value ϕ_0 , which can also vary with time. Slow variations in ϕ_0 due to small radial movements in the cut-off layer can modulate the total signal $S(t)$ and its spectrum by changing the reflectometer sensitivity in the cosine term.

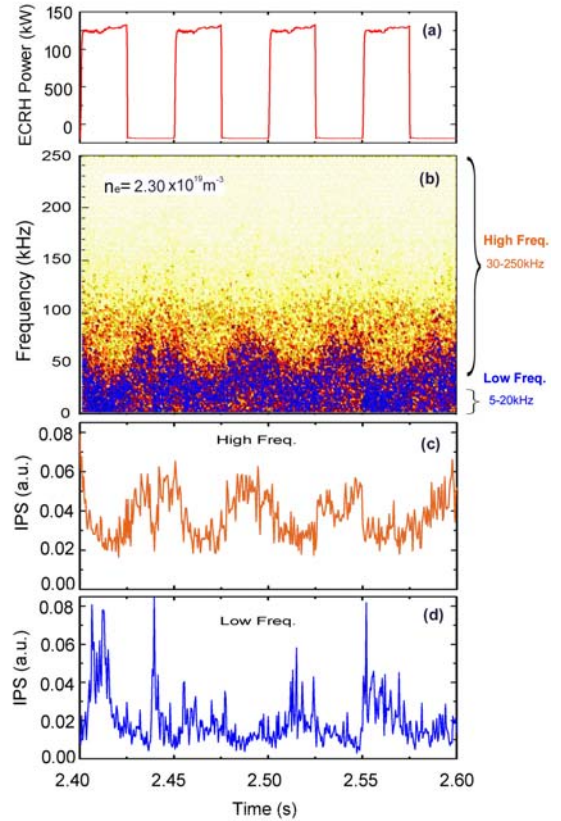


Fig. 4.25 – Temporal evolution of: (a) ECRH power; (b) power spectrum from the 43 GHz ($n_e=2.3 \times 10^{19} \text{ m}^{-3}$) reflectometer channel; and integrated power spectrum over the frequency bands [30,250] (c) and [5,20] kHz (d), respectively, for AUG discharge 13174. As before, the contour plot colour scale is linear going from lighter to darker colours with increasing spectral intensity.

This is illustrated in Fig. 4.28a which presents the raw signal $S(t)$ from the same edge channel shown in Fig. 4.26, together with the radial position of the plasma boundary (separatrix R_{sep}) deduced from magnetic diagnostics (Fig. 4.28b). The envelope of the reflected signal is modulated in agreement with the changes in bulk plasma position. The modulation in $S(t)$ envelope also corresponds to the modulation in its spectrum shown in Fig. 4.26b. The modulation in the plasma boundary (Fig. 4.28b) appears due to the feedback control system in the main power supply which has a natural oscillation frequency of ~ 25 Hz generating a modulation in the bulk plasma position

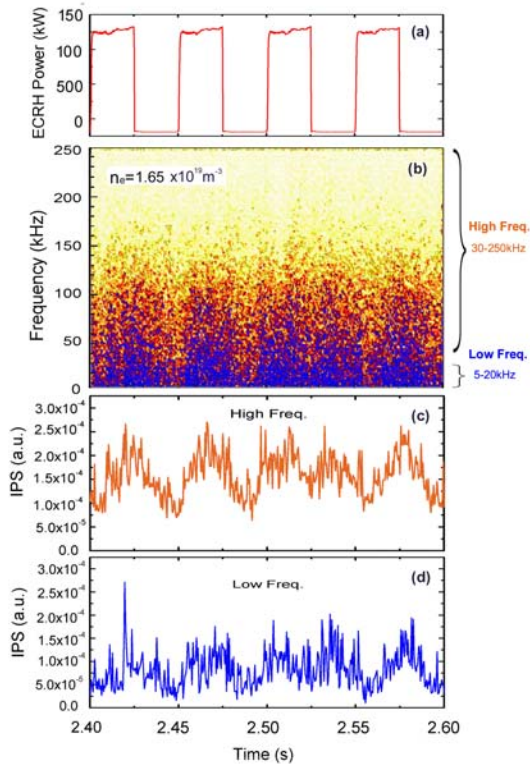


Fig. 4.26 – (a) ECRH power (b) Power spectrum from the 36.5 GHz ($n_e = 1.65 \times 10^{19} \text{ m}^{-3}$) reflectometer channel for shot 13174, with IPS for [30,250] kHz (c) and [5,20] kHz (d) frequency bands. The cut-off layer is approximately $\rho \sim 0.95$. The colour scale for the contour is linear going from lighter to darker colours with increasing spectral intensity

with an amplitude of ~ 2 mm. This displacement is comparable to the reflectometer microwave wavelength and is therefore seen by the diagnostic. The instrumental sensitivity due to radial cut-off movements are particularly important because the typical frequency of the feedback system (~ 25 -30 Hz) is very close to the ECRH modulation frequency. Although bulk plasma movement may account for the

modulation in the edge channel spectra, it can not explain the behaviour of the high and low frequencies seen only in the ECRH modulation experiments.

The results suggest that the ECRH affects locally the level of higher frequency plasma turbulence (above 30 kHz), as this part of the spectrum shows good temporal correlation with the heating pulses for different discharges. The modulation in the lower part of the spectrum (5-20 kHz) seem to result from a combination of ECRH (physical) and cut-off layer movements (instrumental) effects. The distinct behaviour of high/low frequencies might be explained by a simultaneous increase in the high frequency turbulence level (ECRH) and decrease of diagnostic sensitivity (leading to an apparent decrease in the low frequencies). Further evidence for this enhancement is seen in discharge 12453 (Fig. 4.27) where a clear increase in the energy for the higher frequencies (above 30 kHz) occurs after a second ECRH gyrotron is applied (with constant $P=400$ kW) in addition to the 30 Hz modulation pulses.

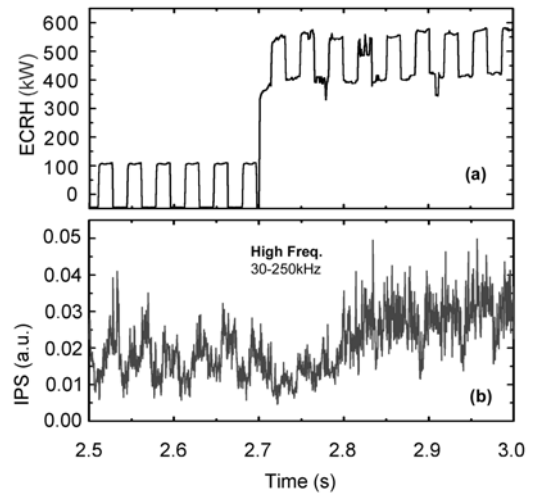


Fig. 4.27 – Temporal evolution of: (a) ECRH power and (b) IPS over the frequencies [30,250] kHz for discharge 12453; the deposition for modulated gyrotron is around $\rho_{pol} \approx 0.86$ and $\rho_{pol} \approx 0.5$ for the second. The line average density and electron density profiles given by DCN+Li beam show no significant change during this interval

However, alternative explanations may not be excluded at the moment. ECRH deposition might also cause: (a) local changes in plasma rotation, generating Doppler shift effects in the signal measured by the reflectometer; (b) energy cascade processes between high and low frequencies, related with changes in the turbulence scale length. Future

experiments will attempt probe the inner layers, to check the suggested transport decrease in this region.

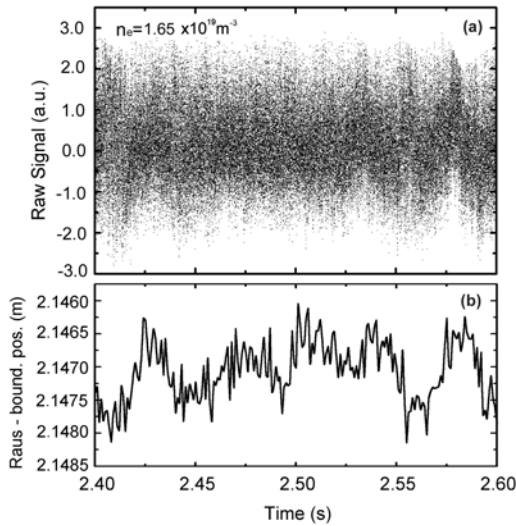


Fig. 4.28 – (a) Raw signal from 43 GHz ($n_e = 2.3 \times 10^{19} \text{ m}^{-3}$) reflectometer channel and (b) radius of plasma separatrix (R_{sep}) for discharge 13174. Note how R_{sep} correlates with the low frequency modulation of the reflectometer signal envelope

4.2.6. ITER relevant studies

The following ITER relevant studies were carried out in 2000:

- Experimental and simulation studies to interpret the signatures of the MHD modes on the broadband reflectometry signals in order to localize the resonance surfaces with enhanced MHD activity.

The main objective is to investigate the possibility of using reflectometry to estimate the q-profile and its modifications, in particular in scenarios with reversed magnetic field, leading to internal transport barriers.

- Measurements on edge plasma position aiming to demonstrate that reflectometry signals can be used in feedback loops for machine protection and plasma control, in long pulse operation, when magnetics may accumulate significant errors.

First results obtained in ASDEX Upgrade show that plasma movements could be followed from the direct measurement of the distance between the edge plasma and the machine wall (see section 4.2.4.2).

- Study of a method based on a neural network approach to reduce the computation time needed for evaluation of edge plasma position to times compatible with the control requirements.

A software work frame allows the easy generation of simulated signals to set-up a profile database, taking into account typical fusion density profiles. Different noise sources/types could be implemented and the results are generated and plotted automatically. This profile database will be crucial to test the crucial approach.

4.3. REFLECTOMETRY ON TJ-II

4.3.1. Introduction

The following main activities were performed in 2000:

- Analysis of the frequency results showing the effect of heating on the plasma turbulence
- Assessment of the problems detected in broadband operation: lost of signal, noisy signals and spurious fringes.
- Study of a new installation of the system in the stellarator hall to minimize the effect of ground loops, that are likely to be the cause of significant electric noise that is preventing to obtain good results.
- Development of a sweep signal switcher to enable sequential sweeping of different frequency bands without dead time between band segments.

4.3.2. Ramp switching circuit

The ramp switching circuit (Fig. 4.29) allows the fast ($< 1 \text{ ns}$) switching between the two microwave channels. The circuit is built around a fast current feedback amplifier. A simple TTL logic is used to decode the signals from the amplifier that will follow the ramp signal to the adequate HTO driver. At the same time a microwave switch uses the same decoded signals to select the input of the right frequency multiplier. The overall bandwidth exceeds 30 MHz, with a gain of one.

4.4. REFLECTOMETRY ON MAST

The following main tasks were carried out during 2000:

- Construction of microwave antennas. The antennas were built and successfully tested and they were mounted in the in-vessel flange. The microwave circuits between the cubicle and the vacuum flange were tested and the reference pins were adjusted with a metallic mirror. The system is now ready for installation in the MAST tokamak, expected for March 2001, shortly before MAST will resume operation.

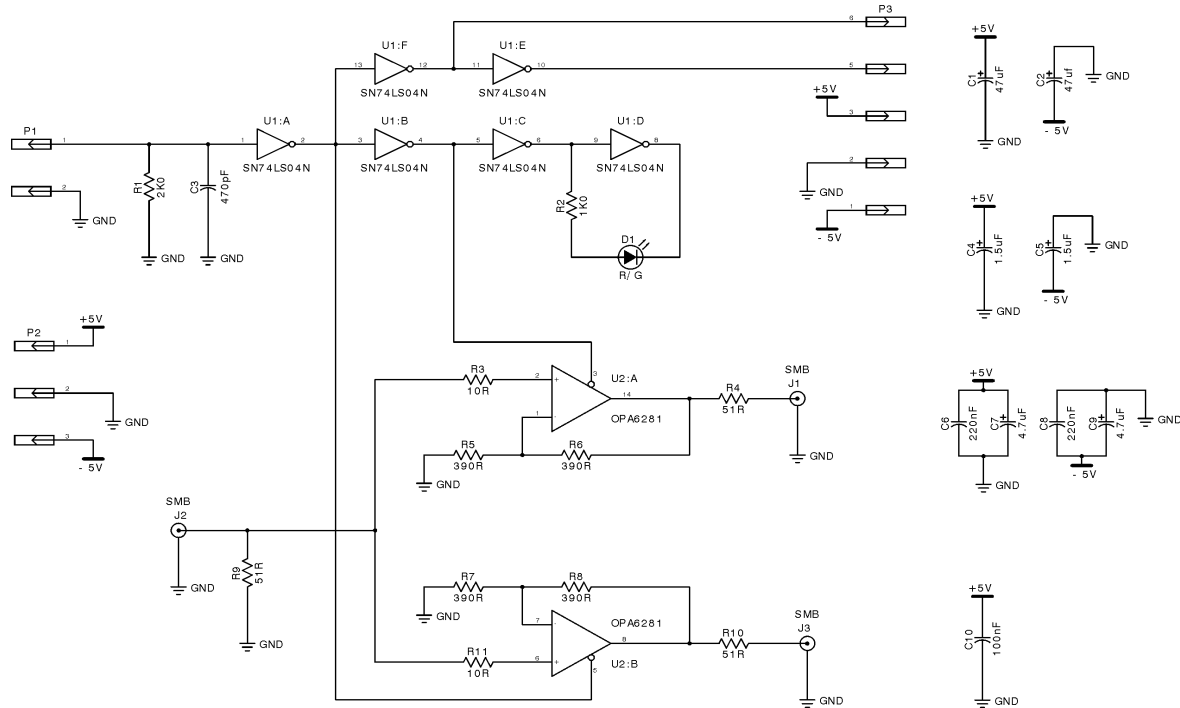


Fig. 4.29 – Fast edge HTO tuning ramp switch.

- Construction of the drivers and the power supplies for the microwave generators as well as the detections amplifiers.
- Assessment of the conditions required for the integration of the data analysis tool in the MAST data acquisition environment.
- Selection and ordering of the HTO oscillators.

4.5. REFLECTOMETRY FOR ITER

Besides the studies referred to in section 4.2.6, the following main tasks were also performed during 2000:

- Participation in the EU-ITER Progress Meeting on Diagnostics, where it was presented (by Manso and Sanchez) the progresses on present EU machines relevant for ITER-FEAT.
- Acceptance of major responsibility (CIEMAT will be the other partner) in the Design Task to re-evaluate the conceptual design of reflectometry for ITER presented in DDD 5.5.F.02 in the FDR and to assist the JCT in the updating of documentation, including costing of the system. A first visit was made to the CSU-Garching to obtain technical information relevant for the Task.

- Elaboration of the content of a R&D Task entitled “Construction and Test of a Typical Microwave Run”, (Work order under T486 - Phase 1), aiming at designing, constructing and optimizing a complex transmission line, which will be a crucial item for the implementation of reflectometry on ITER-FEAT.
- Elaboration of a proposal to the SAPIENS-99 programme to seek finance support for the Portuguese contribution (~150 000 ECU) to participate in the above R&D task, which failed to get approval.

4.6. NUMERICAL CODES

4.6.1. Introduction

The following main activities were carried out in 2000:

- Development of a Finite Difference Time Domain two dimensional code suited for broadband O-mode reflectometry
- Application of this code to the study of typical features encountered on the ASDEX Upgrade discharges.
- Beginning of a collaboration between IST and various French research organisms: CEA, CNRS and Universities of Marseille and Nancy.

4.6.2. 2D full-wave FDTD Maxwell code for simulation of CW-FM broadband reflectometry

A two-dimensional full-wave finite-differences time-domain Maxwell code for simulation of reflectometry experiments has been developed as a tool to help the understanding and interpretation of the complex response obtained in reflectometric experiments. This is the first code that simulates CW-FM broadband reflectometry, with emphasis on density profile measurements. The code solves the Maxwell curl equations for ordinary mode propagation in a cold plasma in the x - y plane with no gradients in the z axis and the plasma static magnetic field assumed in the z direction. Plasma effects have been included in the response of the density current to the electric field. The equations are solved on a computational grid where absorbing boundary conditions have been imposed (Higdon's method). Plasma is modelled along curves of isodensity. The code uses a single antenna both for emission and reception mimicking the one-antenna set up used at ASDEX Upgrade (Fig. 4.30).

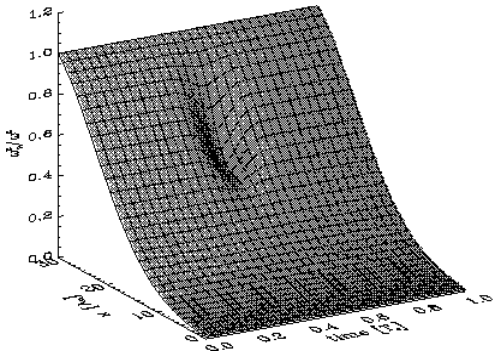


Fig. 4.30 – Contour plot of the positive half of the electric field

Signal is injected in the system by exciting a grid point with a modulated frequency signal, being the output signal monitored at the same point. Homodyne detection scheme is used to obtain the reflectometric signal which may, then, be treated using the same methods applied to the experimental data.

To simulate plasma movements a perturbation, varying in time and space, is added to the static plasma. The code was used to study typical situations of fusion plasmas when a rotating magnetic island is present (Figs. 4.31 and 4.32) and during an ELM (Fig 4.33).

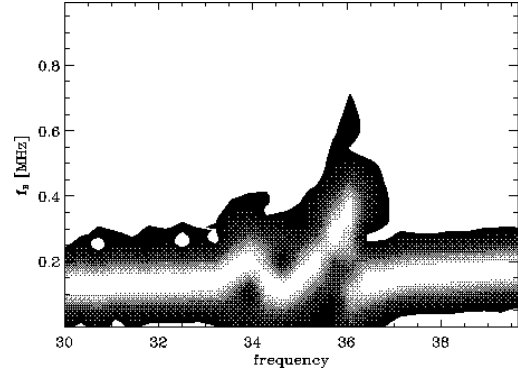


Fig. 4.31 – Rotating density plateau – temporal evolution of ω_p^2/ω^2

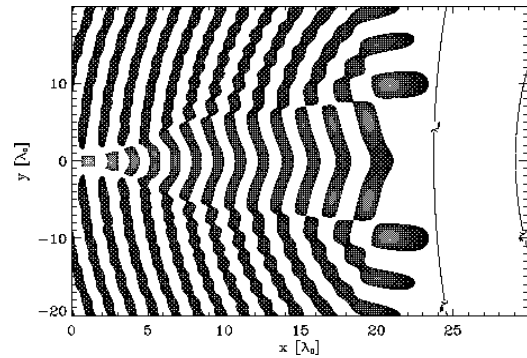


Fig. 4.32 – Frequency-time distribution of the simulated signal for a rotating density plateau.

The numerical studies are in good agreement with the experimental results on ASDEX and ASDEX Upgrade.

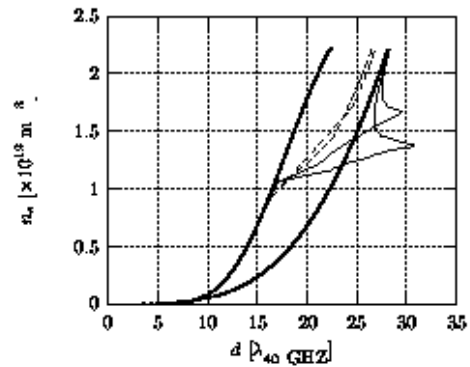


Fig. 4.33 – Reconstructed density profiles

4.6.3. Investigation of MHD modes on ASDEX Upgrade using a 1D code

The purpose of this study is to investigate the influence of large-scale radial structures on the reconstruction of density profiles using microwave reflectometry.

The simulation code used for this study is a code developed by Holzhauser based on an equivalent electrical network, that models the stationary background plasma with a gaussian density perturbation, with a certain frequency of rotation and amplitude. In this model the impedance of transmitter/receiver antenna is matched to vacuum outside the SOL (Scrape-Off Layer) to ensure that the reflected wave is perfectly absorbed at the antenna mouth.

For the simulation of a magnetic island realistic parameters were used based on an ASDEX Upgrade discharge. The rotation frequency of the island is 11.5 kHz with a size of 5 cm and a swept rate of 20 μ s. Figs. 4.34 and 4.35 show two curves of group delay (τ_g) (1) and corresponding reconstructed profiles (2) for two different times of acquisition.

The group delay was computed from the phase signal obtained with the code. In this figures a discontinuity at band interface and a peak at 42 GHz ($\sim 2.2 \times 10^{19} \text{ m}^{-3}$) is observed.

The experimental results were obtained using the O-mode broadband channels and the Q fluctuations monitor, probing density was $n_e \approx 2.2 \times 10^{19} \text{ m}^{-3}$. The broadband channels probe sensitive in the range ($0.3 \times 10^{19} \text{ m}^{-3}$ to $6.64 \times 10^{19} \text{ m}^{-3}$) at both HFS and LFS. The signals were acquired in burst of 32 sweeps each spaced by 10 μ s using an acquisition time of 20 μ s.

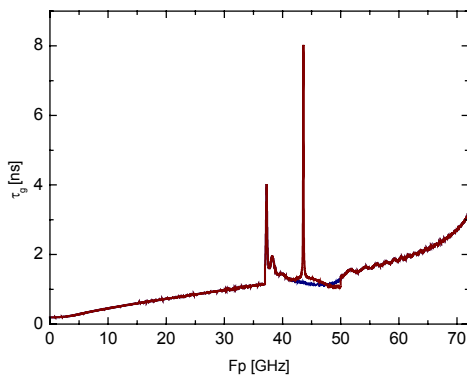


Fig. 4.34 – Group delay computed from phase signal obtained with 1D code

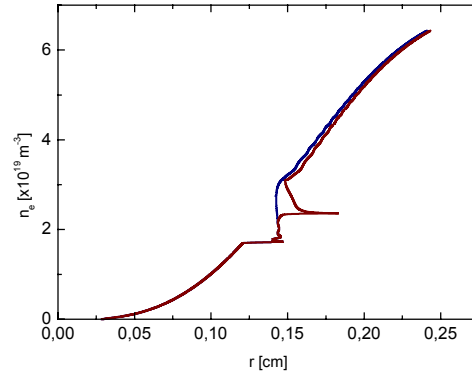


Fig. 4.35 – Reconstructed density profiles

The discharge under study is a medium triangularity H-mode discharge with a locked mode at ~ 2.8 s (#11694). In Figs. 4.36 and 4.37 the curves of group delay and the corresponding reconstructed density profiles are shown. It can be seen that, as in the simulation, there is a discontinuity between two bands (Ka and Q) and that also a peak at ~ 42 GHz appears. The red and blue curves show the maximum and minima island perturbation respectively. From Fig. 4.36 a peak at 42 GHz is seen in only one of the τ_g curve and a jump is found in both curves.

This leads to a conclusion that the amplitude changes with time/phase of the island and that in this case there is a discontinuity between Ka and Q bands. As seen in Fig. 4.36, the peak appears as a moving hole in the density profile and the discontinuity appears as a flattening. This flattening may not be

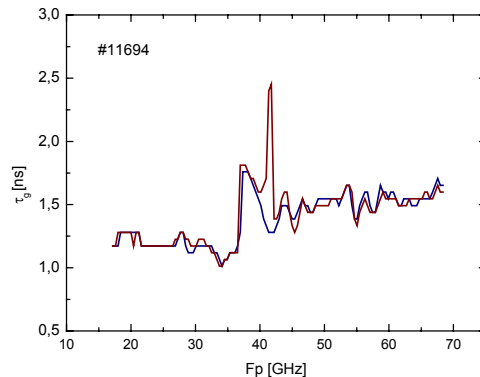


Fig.4.36 - Curves of group delay

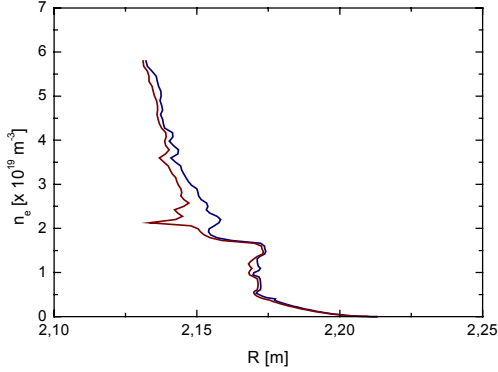


Fig. 4.37 - Corresponding reconstructed profiles

real, can be due to the jump when connecting bands. In this case, as we will show in Fig. 4.38, this jump is constant through all the sweeps, which may indicate that it can be real, it can be due to the magnetic island. Fig. 4.38 presents a contour plot of the group delay. As can be seen there are eleven peaks at $n_e \sim 2.2 \times 10^{19} \text{ m}^{-3}$ which occurs at a frequency of 11.5 kHz. The peak shown before in Fig. 4.36a) (red curve) correspond to one of the peaks in this figure (red colour – highest τ_g). As said before the jump between bands remains constant through all the sweeps. Fig. 4.38 shows results from the fluctuations monitor channel and the magnetic probes.

Fig. 4.39a depicts the spectrogram (linear scale) of reflectometry fluctuations from 42 GHz LFS channel and Fig. 4.39b the corresponding magnetic fluctuations from Mirnov coils. Clear MHD features at 11.5 kHz in both reflectometry and magnetics results are seen plus harmonics and sub harmonics. As told before the mode locks at 2.8 s, which can also be clearly seen. Vertical bars in Fig. 4.39 show the acquisition times of 2 bursts of 32 profiles. The first burst at the start of mode and the second burst at the time of locking.

4.6.4. Collaboration with French Institutions

A first meeting between the Portuguese and French teams was held in Lisbon (9-10 November 2000) to discuss the numerical results and to plan the work to be done in the frame of this collaboration.

First results were obtained on the application of a simple model, based on the Doppler frequency shift due to the plasma poloidal rotation in the cut-off layer, which can reproduce qualitatively the results on ASDEX Upgrade. The frequency shift towards the high frequency range observed with this model corresponds to an appearance of string rotation shear in the cut-off layer probed by reflectometry.

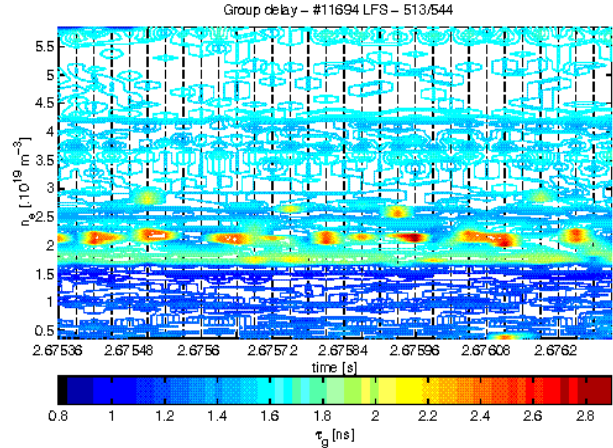


Fig. 4.38 – Contour plot of the group delay representing 32 sweeps spaced by $10 \mu\text{s}$. The total time is $960 \mu\text{s}$.

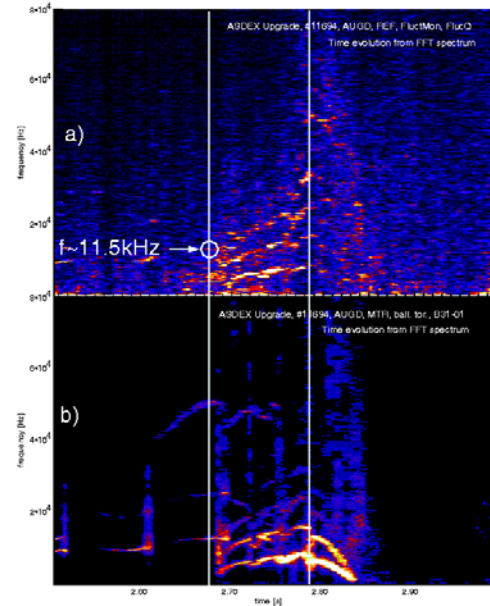


Fig. 4.39 – Time evolution of a) fixed frequency signal and b) Mirnov coils